Earth and Planetary Science Letters 396 (2014) 165–178

Contents lists available at ScienceDirect

Earth and Planetary Science Letters

www.elsevier.com/locate/epsl

Pore pressure distribution of a mega-splay fault system in the Nankai Trough subduction zone: Insight into up-dip extent of the seismogenic zone

Takeshi Tsuji [a,*], Rie Kamei [b,c], R. Gerhard Pratt [b]

[a] International Institute for Carbon-Neutral Energy Research (WPI-I2CNER), Kyushu University, Fukuoka, Japan
[b] Department of Earth Sciences, University of Western Ontario, London, Ontario, Canada
[c] University of Western Australia, Crawley, Australia

ARTICLE INFO

Article history:
Received 22 January 2014
Received in revised form 2 April 2014
Accepted 5 April 2014
Available online 25 April 2014
Editor: P. Shearer

Keywords:
mega-splay fault
pore pressure
Nankai Trough
rupture propagation
waveform tomography

ABSTRACT

We use the pore pressure distribution predicted from a waveform tomography (WT) velocity model to interpret the evolution of the mega-splay fault system in the Nankai Trough off Kumano, Japan. To map pore pressure around the mega-splay fault and plate boundary décollement, we integrate the high-resolution WT velocities with laboratory data and borehole well log data using rock physics theory. The predicted pore pressure distribution shows that high pore pressures (close to lithostatic pressure) along the footwall of the mega-splay fault extend seaward to the trough region, and the normalized pore pressure ratio is nearly constant over that extent. This continuity of the overpressured zone indicates that a coseismic rupture can potentially propagate nearly to the trough axis. We interpret a high-pressure belt within an accretionary wedge on the landward side of the present mega-splay fault as evidence of the ancient mega-splay fault. Because the ancient mega-splay fault soles into the active mega-splay fault, the active mega-splay fault may function as a basal detachment fault and is directly connected to the seaward plate boundary décollement.

1. Introduction

Earthquakes at convergent plate margins frequently occur at plate interfaces or on splay faults that branch from the interfaces and propagate upward into an overlying wedge (e.g., Park et al., 2002). The structure of these seismogenic faults have been characterized in many subduction zones primarily using seismic images of the tectonic structures (e.g., Kopp et al., 2009; Kopp, 2013; Moore et al., 2009; Ranero and von Huene, 2000; Van Avendonk et al., 2013). Pore pressure distributions around the faults are also a key to understanding coseismic rupture propagation (e.g., Kimura et al., 2012; Moore and Saffer, 2001; Scholz, 1998). Various studies have estimated pore pressure conditions, but these have mostly been limited to the areas around plate boundary décollements near the trough axes (e.g., Bangs et al., 1999; Cochrane et al., 1994; Hayward et al., 2003; Shipley et al., 1994; Westbrook, 1991; Tobin and Saffer, 2009; Tsuji et al., 2008). A lack of accurate estimations of pore pressure from the deeper parts of mega-splay faults has precluded the prediction of pore pressure variations extending from deep mega-splay faults to shallow plate boundary décollements. The variations in pore pressure are crucial in the evaluation of coseismic rupture propagation (e.g., Conin et al., 2012) and the up-dip limit of the coseismic region (Moore and Saffer, 2001; Kimura et al., 2012).

The Nankai subduction zone where the Philippine Sea plate is subducting beneath the Japanese Island at approximately 4–6.5 cm/s (Fig. 1; Seno et al., 1993; Miyazaki and Heki, 2001) is a well studied plate convergent margin (e.g., Bangs et al., 2009; Moore et al., 2009; Park et al., 2010; Tobin et al., 2009). In this convergent margin, great earthquakes in excess of M_w 8 have occurred repeatedly (Ando, 1975) and caused large damage to mega-cities on the Japanese Island. Because of the high seismic risk, geophysical and drilling data have been intensively acquired in the Nankai accretionary prism. Several studies have mapped pore pressure distributions within the accretionary prism seaward of the mega-splay fault (i.e., the outer wedge in Fig. 2b) either using borehole data (e.g., Saffer, 2003; Screaton et al., 2002), or using seismic reflection data (e.g., Tobin and Saffer, 2009; Tsuji et al., 2008). These studies show evidence of high pore pressures beneath the plate boundary décollement near the trough axis.

* Corresponding author at: International Institute for Carbon-Neutral Energy Research (WPI-I2CNER), Kyushu University, 744 Motooka, Nishi-ku, Fukuoka 819-0395, Japan. Tel.: +81 92 8026875; fax: +81 92 8026875.
E-mail address: tsuji@i2cner.kyushu-u.ac.jp (T. Tsuji).

http://dx.doi.org/10.1016/j.epsl.2014.04.011

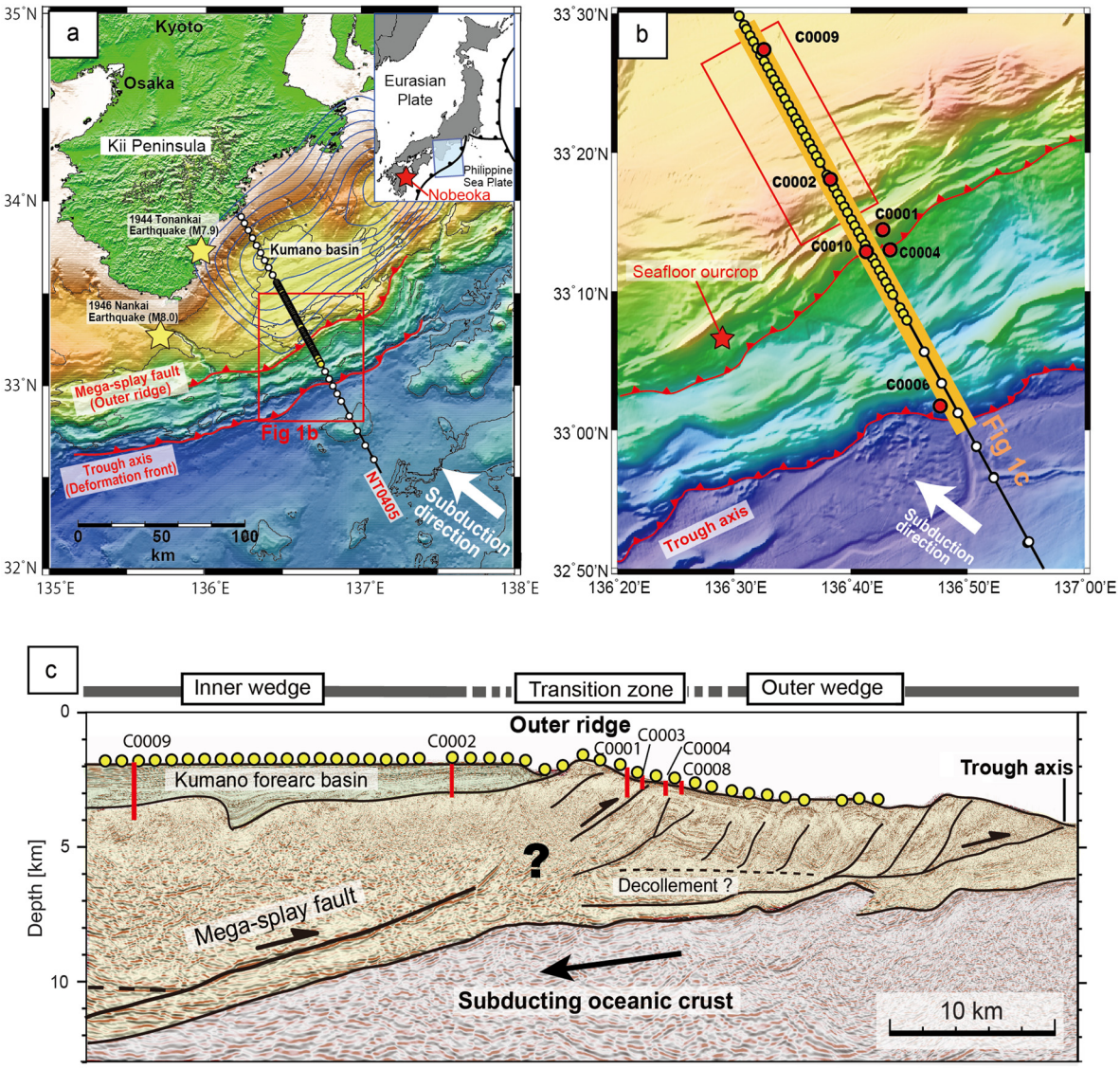

Fig. 1. (a) Seafloor topography in the Nankai Trough off Kumano with survey line location (NT0405). Blue contours show the coseismic slip distribution of the 1944 Tonankai earthquake (0.5 m increment; Kikuchi et al., 2003). Yellow stars show the hypocenters of the 1944 Tonankai earthquake and the 1946 Nankai earthquake. Red star indicates the locations of the Nobeoka thrust. (b) Enlarged seafloor topography around the survey area off Kumano. White and yellow circles on the solid black line indicate OBS positions; yellow circles indicate the OBSs used for Waveform Tomography analysis and correspond to the survey area displayed in Fig. 2(b). The red rectangle corresponds to the area shown in Fig. 8. The red star and circles indicate the locations of seafloor outcrop for rock sampling and boreholes. (c) Seismic reflection profile extracted from 3D seismic volume. The location of this seismic profile is approximately that of the OBS survey line (orange line in panel (b)).

In spite of the extent of the seismic data from the Nankai subduction region, unfortunately the signal-to-noise ratio of the reflection seismic data within the accretionary prism is low on the landward side of the mega-splay fault (Fig. 1; Moore et al., 2009), probably owing to rock consolidation and complicated geological structures. As a result of these data problems, the evolution of the mega-splay fault system cannot be interpreted from reflectivity data alone. Furthermore, the deeper part of the mega-splay fault (approximately 10 km in depth) is too deep to estimate reliable seismic velocities from short-offset (i.e., offsets of less than 6 km) reflection data (Yilmaz and Doherty, 2001), thus to date it has not been possible to predict pore pressures around the mega-splay fault where coseismic slip has believed to occurred (Kikuchi and Yamanaka, 2001; Kikuchi et al., 2003). Seismic velocities for the deep lithology can be revealed by applying traveltime tomography to long-offset ocean bottom seismometer (OBS) data (Nakanishi et al., 2008; Takahashi et al., 2002), but the resolution is typically limited to larger than approximately 1 km, which is not enough to characterize the pore pressure variations along the mega-splay fault.

The existing reflection images also poorly characterized the transition zone between the mega-splay fault developed in the landward inner wedge and the décollement in the seaward outer wedge (Figs. 1b and 2b), due to seafloor multiples that obscure the structural signature of this area (Moore et al., 2009; Yilmaz and Doherty, 2001). The structures and pressure conditions of the transition zone are critical for evaluating the possibility of the coseismic rupture propagation close to the trough axis (e.g., Wang and Hu, 2006). This rupture propagation may trigger large tsunamis, both because the seafloor slope is steeper on the seaward side of the transition zone (Satake, 1994; Tanioka and Satake, 1996) and because the uplift of the deep seafloor near the trough axis amplifies the height of the tsunami (Ryan et al., 2012). The mega-splay fault reaching the seafloor in the transition zone is believed to have ruptured during the 1944 Tonankai earthquake (e.g., Kikuchi and Yamanaka, 2001). However, the 1605 Keicho earthquake (M_w 7.9), was interpreted to have generated coseismic

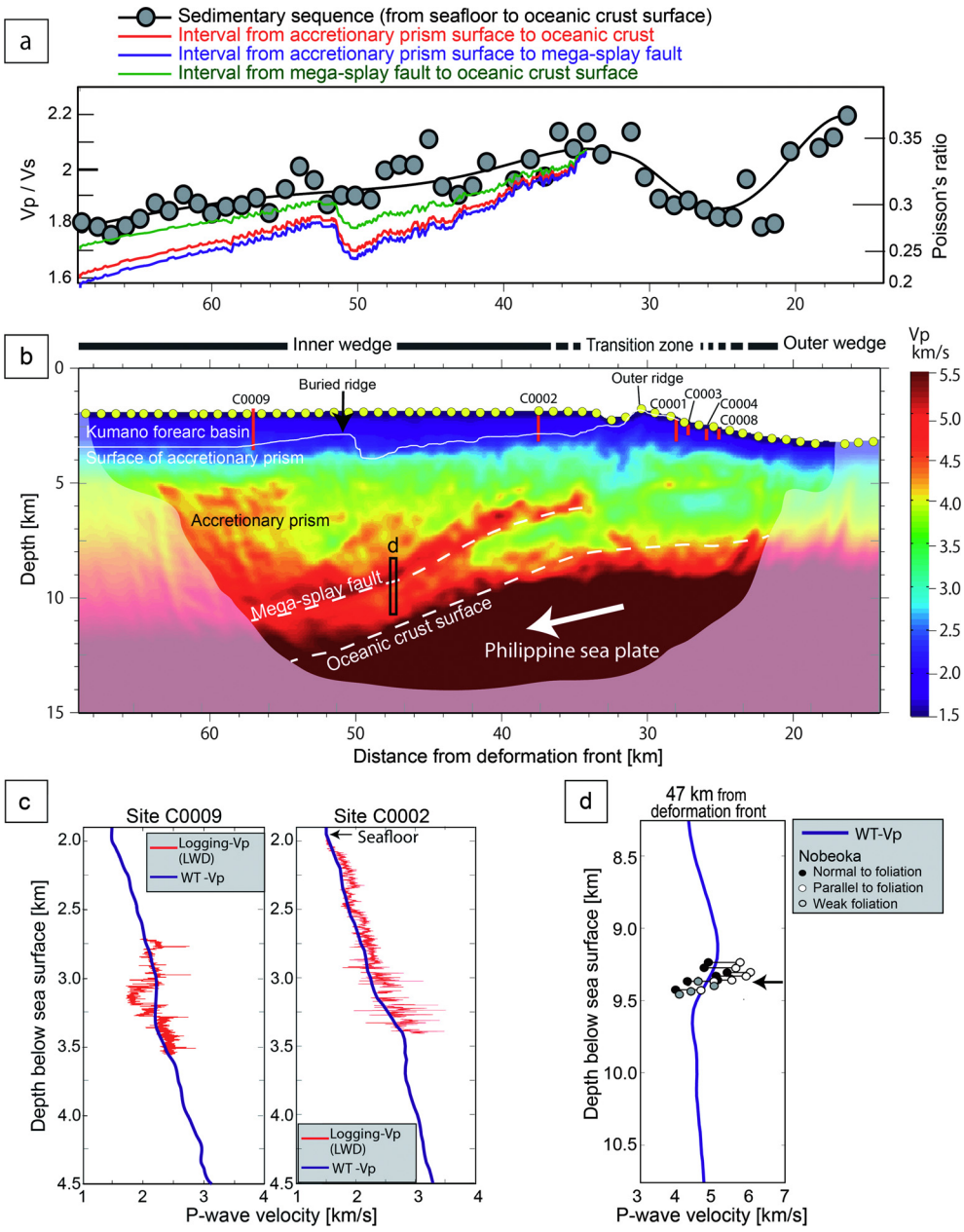

Fig. 2. (a) Vp/Vs ratio above the subducting oceanic crust surface (within sedimentary sequence) estimated from P-to-SV converted wave (gray circles; Tsuji et al., 2011). Red line indicates the Vp/Vs ratio from the accretionary prism surface to the oceanic crust surface. The blue line indicates the Vp/Vs ratio within accretionary prism (from the accretionary prism surface to the mega-splay fault). Green line indicates Vp/Vs ratio of underthrust sequence (from the mega-splay fault to the crust surface). (b) P-wave velocity obtained by Waveform Tomography analysis. The velocity model is a little different from that of Kamei et al. (2012, 2013); the model is less contaminated by artifacts and is more suitable for pore pressure prediction. Areas with poor wavepath coverage are indicated by reduced opacity. Yellow circles show location of the OBS used for analysis. Red lines indicate borehole locations. Black rectangle indicates the location of the velocity profile displayed in panel (d). (c) P-wave velocity obtained by logging (red line; Tobin et al., 2009; Saffer and et al., 2009) and Waveform Tomography (blue line). (d) P-wave velocity of the Nobeoka fossil mega-splay fault measured at 55 MPa (circles; Tsuji et al., 2006) and Waveform Tomography (blue line). Black arrow indicates the location of the fault core of the Nobeoka thrust. (For interpretation of the references to color in this figure legend, the reader is referred to the web version of this article.)

rupture close to the trough axis, because the earthquake had a small seismic intensity but caused a significant tsunami (Ishibashi, 1983; Seno, 2002). The tsunami of the 2011 Tohoku earthquake was also generated by rupture propagation close to the trench (e.g., Fujiwara et al., 2011; Ito et al., 2011; Tsuji et al., 2013a).

In this study, we estimate a high-resolution seismic velocity distribution by applying frequency-domain waveform tomography (WT; e.g., Brenders and Pratt, 2007; Kamei et al., 2012, 2013) to a long-offset OBS data set from the Nankai Trough off Kumano, where both the 1605 Keicho earthquake and the 1944 Tonankai earthquake occurred. The WT method allows us to estimate velocities in the deeper part of the mega-splay fault, where previous models have been somewhat obscure. We then predict pore pressures around the Nankai mega-splay fault from the seismic velocity model in order to explore the evolution of the mega-splay fault and its relationship to the plate boundary décollement.

Many previous studies have relied on empirical relationships to predict pore pressure from seismic velocities (e.g., Eaton, 1972; Eberhart-Phillips and Han, 1989; Dutta, 2001). If the sedimentary sequence is stratified and many boreholes penetrate it, we can estimate pore pressure by comparing an abnormal compaction trend with a normal compaction trend or by assuming a compaction

disequilibrium regime (e.g., Rubey and Hubbert, 1959; Eaton, 1972). However, only a limited number of deep boreholes penetrate the Nankai accretionary prism, which becomes progressively more consolidated and cemented in the landward direction (e.g., Morgan et al., 2007). Thus it is difficult to define an appropriate normal compaction trend in the accretionary wedge. Furthermore, high-pressure fluid intervention due to clay dehydration (e.g., Powers, 1959) or fluid migration (e.g., von Huene and Lee, 1982) decreases seismic velocities without much change in porosity, because the unloading procedures open thin cracks in the rocks with low porosity (e.g., Kuster and Toksoz, 1974). Therefore it is difficult to predict pore pressure in the deeper parts of the mega-splay fault. Instead of using normal compaction trends or assuming a compaction disequilibrium regime, pore pressure should be estimated by using a relationship between seismic velocity and effective stress for each lithology (Carcione et al., 2003). To predict pore pressure of the deeper part of the mega-splay fault, therefore, we adopt an established rock physics method and construct the relationship between seismic velocities and effective stress (Tsuji et al., 2008). The approach allows us to effectively integrate the laboratory-derived properties for pore pressure prediction.

2. Data for pore pressure prediction

2.1. High-resolution P-wave velocity derived from waveform tomography

We use the previously published method of Kamei et al., (2012, 2013) to extract a P-wave velocity model of the mega-splay fault system from controlled-source OBS data acquired off Kumano (Nakanishi et al., 2008). The WT method retrieves velocity information from refracted and wide-angle reflected waves by exploiting seismic waveforms beyond the first arrival times, and achieves much higher resolution than conventional traveltime tomography methods (Fig. 2b). The long-offset OBS data (data with offsets up to 55 km were available for the inversion) allows the method to estimate velocity structures as deep as 12 km below the sea surface, including the transition zone between the mega-splay fault and the décollement.

In this study, we implemented WT in the frequency domain largely following the approach we described in earlier publications (Kamei et al., 2012, 2013). Starting from the traveltime tomography result of Nakanishi et al. (2008), we iteratively updated the velocity model to minimize waveform misfits in phase using the local non-linear conjugate gradient method. To mitigate the non-linearity and non-uniqueness of the inversion, we started the inversion by fitting the lowest-frequency components of the recorded data (2.25 Hz), then sequentially incorporated the higher-frequency components up to 8.75 Hz. This progressive frequency schedule (Kamei and Pratt, 2012) differs from the sequential frequency schedule used in Kamei et al., (2012, 2013), in which we discarded the low-frequency components from the inversion when inverting for the higher-frequency components. The progressive frequency schedule allowed us to maintain the fitness of the low-frequency data throughout the inversion, further stabilizing the inversion. As a result, the velocity model is less contaminated by artifacts and is more suited for pore pressure prediction than the model of Kamei et al., (2012, 2013). From checkerboard tests, the spatial resolution of the retrieved velocity model was estimated to be 350 m in the vertical direction and 700 m in the horizontal direction (Kamei et al., 2012, 2013).

2.2. Vp/Vs ratios for elastic moduli calculation

The P-wave to S-wave velocity ratio, Vp/Vs ratio (or Poisson's ratio), can be used to increase the accuracy of pore pressure estimates, because the S-wave velocity strongly decreases with pore pressure (Dvorkin et al., 1999). We use the Vp/Vs ratio derived mainly from P-to-SV waves converted at the oceanic crust (Fig. 2a; Tsuji et al., 2011), to calculate the S-wave velocity from the P-wave velocity model derived from WT (Fig. 2b). The Vp/Vs ratio varies along the survey line (Fig. 2a), being larger around the transition zone.

The Vp/Vs ratio estimated from P-to-SV converted waves is an average value over the depth range between the seafloor and the plate interface (Tsuji et al., 2011), which includes the Kumano basin, the accretionary prisms, and the underthrust sediments. The Vp/Vs ratio within of the overlying Kumano basin (above the accretionary prism) was estimated from borehole logging data (Saffer and et al., 2009). In order to obtain the Vp/Vs ratios of the accretionary prism and the underthrust sediments we then recalculated Vp/Vs ratios from accretionary prism surface to the oceanic crust (red line in Fig. 2a) by subtracting the influence of the Kumano basin from the average Vp/Vs ratio. From the amplitude variation with offset (AVO) trend of the seismic reflections, we estimate that the Vp/Vs ratio of the footwall of the mega-splay fault is approximately 1.1 times larger than that of the hanging-wall (Tsuru et al., 2005). By combining this information with the Vp/Vs ratio between the accretionary prism surface and the oceanic crust surface (red line in Fig. 2a), we obtain the Vp/Vs ratio for the accretionary prism and for the underthrust sequence (blue and green lines in Fig. 2a).

2.3. Physical and elastic properties

In modeling pore pressures, we need to use lithologic properties obtained in laboratory experiments and borehole logging. We use elastic velocities and physical properties derived from the borehole logging data acquired during several Integrated Ocean Drilling Program (IODP) drilling campaigns (Expeditions 314 and 319; Tobin et al., 2009) in the Nankai Trough off Kumano (Fig. 1). As sediments in the Kumano basin are at near-hydrostatic conditions at IODP Sites C0002 and C0009 (Saffer and et al., 2009), the confining and effective pressures can be calculated from the density logging data (e.g., Tobin and Saffer, 2009; Tsuji et al., 2008). Therefore, the relationship between seismic velocities and effective pressure at Sites C0002 and C0009 can be derived from the logging data. In addition to the logging data, we use a velocity–effective pressure relationship derived from IODP core samples (Hashimoto et al., 2010; Raimbourg et al., 2011) and from seafloor outcrop samples obtained from the outer ridge using a manned submersible (Tsuji et al., 2008). The velocity–pressure relationship is our primary information for predicting pore pressures from P-wave and S-wave velocity data.

However the boreholes did not penetrate the deeper part of the mega-splay fault, and the properties of these high-porosity shallow rock samples are not representative of those on the deep mega-splay fault (Fig. 1). Thus we substitute the elastic properties of the deeper part of the mega splay fault (i.e., velocity–pressure relationship) with those measured on samples of the fossil mega-splay collected from outcrops at Nobeoka, Kyushu, Japan (Tsuji et al., 2006). The Nobeoka thrust is interpreted to preserve in-situ structures of the mega-splay fault and to be under the temperature and pressure conditions similar to those of the deeper part of the mega-splay fault (e.g., Kondo et al., 2005). The WT-derived P-wave velocity on the deep mega-splay fault is consistent with the laboratory-derived velocity profile (Fig. 2d; Tsuji et al., 2006) and the sonic logging data (Hamahashi et al., 2013) of the Nobeoka thrust. The AVO response estimated from the core samples of the Nobeoka thrust is also consistent with overpressured conditions in the active mega-splay fault (Tsuji et al., 2006). Therefore, we assume that the velocity–pressure relationships of the Nobeoka thrust are representative of the active mega-splay fault. For our analysis, we

use the relationships of the Nobeoka samples measured in dry conditions because in saturated conditions fluid dispersion masks pressure effects, and because velocity is relatively independent of temperature under dry conditions (e.g., Wang, 2001) In our analysis, as described later, we use the curvature gradient of the velocity–pressure relationship of the Nobeoka samples (rather than using the magnitudes of the velocity).

3. Pore pressure prediction methods and results

3.1. Effective-pressure coefficient

We discuss the derivation of pore pressures from effective pressure of the simplest isotropic case (i.e. homogeneous state of stress) before introducing the element of stress. For unconsolidated rocks, the differential pressure P_d governs the pressure dependency of soft rock deformation (Terzaghi, 1936):

$$P_d = P_c - P_f, \tag{1}$$

where P_c is the confining pressure and P_f is the pore pressure. The differential pressure P_d can be estimated from seismic velocity of the unconsolidated rock (e.g., Tsuji et al., 2008). In unconsolidated rock, therefore, pore pressure can be obtained by subtracting the differential pressure from the confining pressure, which in turn can be calculated by integrating bulk density for the vertical direction.

For consolidated rocks, however, the seismic velocity is not solely dependent on differential pressure but, rather, on effective pressure P_e (Biot, 1955; Christensen and Wang, 1985) where

$$P_e = P_c - nP_f, \tag{2}$$

and n is an effective-pressure coefficient (or effective-stress coefficient; e.g., Biot and Willis, 1957; Hoffmann et al., 2005). The coefficient is related to the dry bulk modulus, K_{dry}, and bulk modulus of the frame (mineral modulus), K_m, in static deformations (i.e., deformation with very low frequency) through

$$n = 1 - \frac{K_{dry}}{K_m}. \tag{3}$$

For rocks with high porosity (shallow sequences where K_{dry} is much smaller than K_m in Eq. (3)), the value of the coefficient is close to 1 and the effective pressure is the same as differential pressure (Eq. (1)). For rocks with low porosity (K_{dry} is close to K_m in Eq. (3)), the effective-pressure coefficient is smaller than 1. When the effective-pressure coefficient approaches zero, the pore pressure has little effect on rock deformation (or velocity). Therefore we should consider the coefficient for the estimation of pore pressure around the deeper part of the mega-splay fault.

It should be noted that although Eq. (3) holds only for static measurements and is not strictly applicable to dynamic measurements (e.g., deformation with seismic frequency), the coefficient also plays a strong role even in the dynamic case (Gangi and Carlson, 1996; Prasad and Manghnani, 1997; Carcione et al., 2003). Because the effective-pressure coefficient depends on the deformation behavior of rocks and because deformation of rocks affects bulk modulus and shear modulus differently, the effective-pressure coefficient is different for each elastic property (Hoffmann et al., 2005). Laboratory experiments (using dynamic measurements) demonstrate that the effective-pressure coefficient for bulk modulus is smaller than 1 for consolidated rocks (Hoffmann et al., 2005); n is approximately equal to 0.6 at in situ effective pressures around the deeper part of the mega-splay fault (~50 MPa) and significantly influences to the estimated pore pressure (Carcione et al., 2003). Therefore, using P-wave velocity alone and ignoring the effect of effective-pressure coefficient ($n = 1$), predicted pore pressure should be underestimated at depth. In contrast, the effective-pressure coefficient for the shear modulus is much less sensitive to confining pressure than that for the bulk modulus (Hoffmann et al., 2005). Therefore, S-wave velocities are a more reliable indicator of pore pressure than are P-wave velocities.

In this study, we predict pore pressure distributions from both P-wave velocity and S-wave velocity (shear modulus). Although the effective-pressure coefficient has known to influence to the predicted pore pressure (Eq. (2)), the coefficient is still uncertain in the dynamic case and is difficult to estimate (e.g., Hoffmann et al., 2005). Furthermore, because the coefficient estimated from laboratory experiments differs from that in low-frequency (large-scale) seismic data, we assume that effective-pressure coefficient is one (use Eq. (1)) and try to estimate pore pressure from the S-wave velocity, in addition to using the P-wave velocity.

3.2. Pore pressure estimated at homogeneous state of stress

To estimate effective pressure from seismic velocity, we use the rock-physics based method employed in Tsuji et al. (2008). Pore shapes in consolidated rocks around the mega-splay fault can be modeled by crack-shaped pores (Toksoz et al., 1976). As effective pressure increases, cracks close, and seismic velocities increase (Cheng and Toksoz, 1979). We assume the pore spaces are ellipsoidal, and describe the shapes by their aspect ratio α. Rocks are assumed to contain pores of discrete aspect ratios α_i, represented by an aspect ratio spectrum $c(\alpha_i)$ (Toksoz et al., 1976), where the subscript i is the index for the discrete aspect ratio.

Since the pore concentrations $c(\alpha_i)$ increase logarithmically with aspect ratio for Nankai Trough sediments as in the case of other sandstones (e.g., Cheng and Toksoz, 1979), Tsuji et al. (2008), assumed that

$$c(\alpha_i) = \alpha_i^E \quad \left(10^{-4.8} \le \alpha_i < 1\right), \tag{4}$$

where E is a quantity determined by pore shapes (bounded between zero and one). Lithologies with a large E are dominated by rounded pores with large aspect ratios, whereas mudstone is dominated by thin cracks and has a small E-value. The E-value can be considered to be a parameter controlling the curvature gradient of the velocity–pressure relationship (see Fig. 8 in Tsuji et al., 2008). We model the aspect ratio spectrum $c(\alpha_i)$ by a total of 69 aspect ratios between $10^{-4.8}$ and 1. The pore aspect ratio spectrum for each location (lithology) is determined by multiplying the normalized aspect ratio spectrum by a porosity (Tsuji and Iturrino, 2008). We estimate the porosity from P-wave velocity by using the relationship proposed by Hoffman and Tobin (2004).

To calculate thinner crack closure in the aspect ratio spectrum as a function of differential pressure, we estimate the thinning and closing of cracks as differential pressure increases using the expression proposed by Toksoz et al. (1976) (Tsuji et al., 2008). When thinner cracks are closed, the elastic moduli of the medium are larger. From the aspect ratio spectrum of open cracks at each pressure, the theoretical elastic moduli (P-wave and S-wave velocities) of the medium are calculated using the differential effective medium (DEM) theory (Berryman, 1992). To obtain low-frequency elastic properties, we calculate elastic moduli of the dry frame by using DEM theory, and then calculated the wet moduli by Gassmann fluid substitution (e.g., Mavko et al., 1998). Therefore, by determining the E-value for each lithology, we can calculate the velocity–pressure relationship and estimate pore pressure distribution.

A precise determination of E in Eq. (4) for each lithology requires laboratory experiments on velocity–pressure relationships in borehole samples. In this study, we use the experimental data on

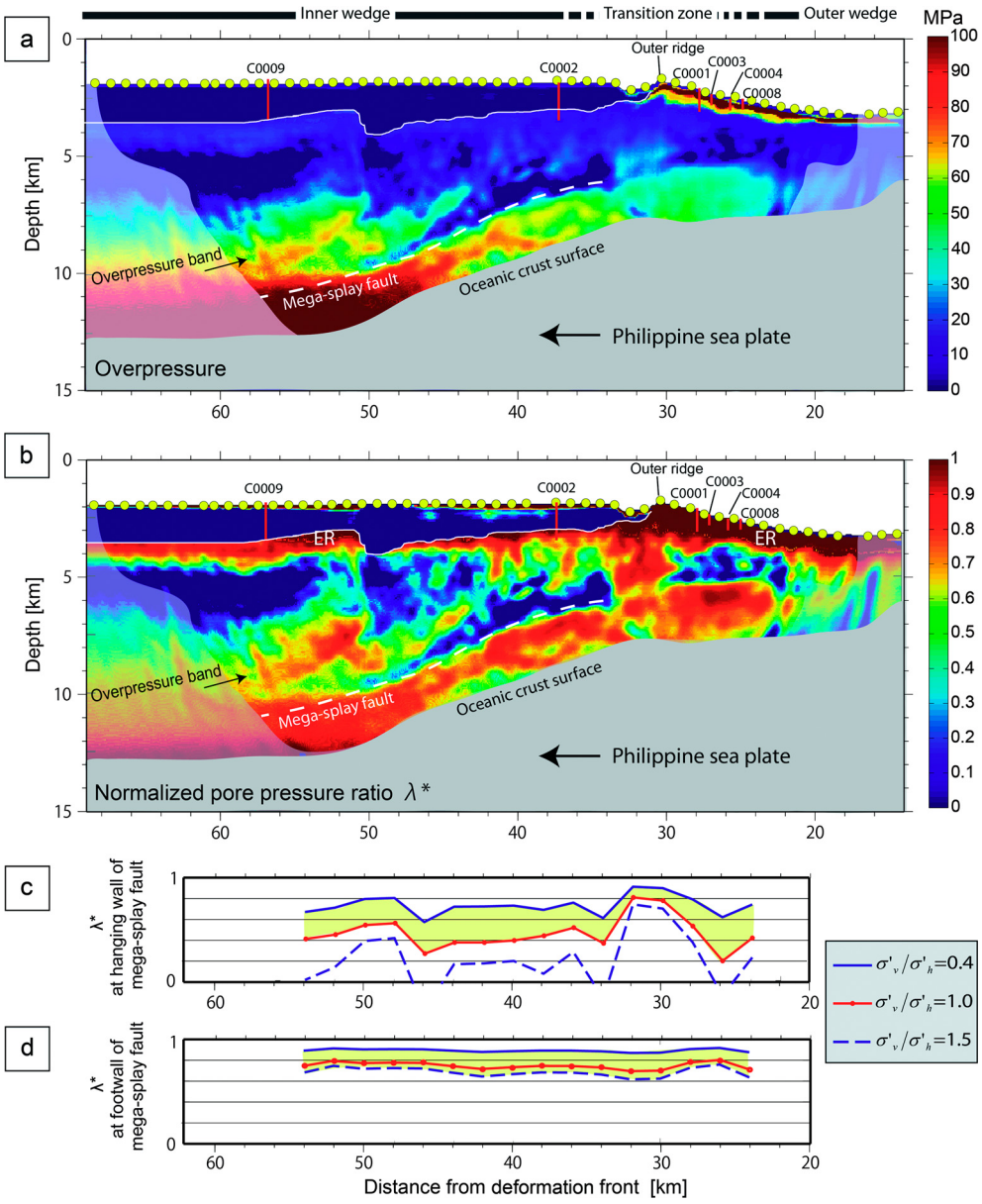

Fig. 3. (a) Overpressure calculated by subtracting hydrostatic pressure from the pore pressure estimated by fitting P-wave velocities. (b) Normalized pore pressure ratio distribution λ^* (Eq. (5)). (c) Normalized pore pressure ratio at the hanging wall of the mega-splay fault (from the accretionary prism surface to the mega-splay fault). (d) Normalized pore pressure ratio at the footwall of the mega-splay fault (from the mega-splay fault to the oceanic crust surface). We display the normalized pore pressure ratio in the case of $\sigma'_v/\sigma'_h = 0.4$ and 1.5 (blue lines) in addition to the result of homogeneous stress state $\sigma'_v/\sigma'_h = 1.0$ (red line). Yellow shaded regions represent the probable range by considering stress state within each lithology. (For interpretation of the references to color in this figure, the reader is referred to the web version of this article.)

rock samples obtained from Sites C0001 and C0002 (Hashimoto et al., 2010; Raimbourg et al., 2011), the seafloor outcrop (Tsuji et al., 2008), and the ancient mega-splay fault at Nobeoka (Tsuji et al., 2006). From porosity, density, sonic velocity, and effective pressure data at Sites C0002 and C0009 estimated as hydrostatic conditions (Saffer and et al., 2009), furthermore, we calculate E-values along the borehole by fitting the experimental and theoretical velocity–pressure relationships. We then determine E-values within the accretionary prism by interpolating and extrapolating values estimated at the boreholes, the outer ridge (from seafloor outcrop samples), and the mega-splay fault (Fig. 2b). Here we assume that E-values of the mega-splay fault (7 to 10 km in depth) are the same as those of the Nobeoka thrust in Tsuji et al. (2008). Although the characteristics of the velocity–pressure relationship vary greatly with lithology, this method can effectively use the information of velocity–pressure relationships in rock samples for pore pressure prediction.

The in-situ effective pressure and pore pressure (Fig. 3) are estimated by fitting the P-wave velocity calculated by DEM theory to the WT-derived velocity distribution in Fig. 2b. However the pore pressure around the deeper part of the mega-splay fault may be underestimated, because P-wave velocities are sensitive to the unknown effective-pressure coefficient n which we assume to be 1 (Eq. (2)). Therefore, we also include S-wave velocity (shear modulus) for pore pressure calculations (Figs. 4 and 5). We use two S-wave velocity models; one derived from the average Vp/Vs ratio within the accretionary and underthrust sequence (red line in Fig. 2a; Fig. 4), and the other from the Vp/Vs ratios separately estimated for the accretionary and underthrust sequence (blue and green lines in Fig. 2a; Fig. 5). Since the overall trends of pore pressure distribution are similar for both cases using S-wave velocity, the 2D profiles of the predicted pore pressure are not shown in Fig. 5 for the latter case.

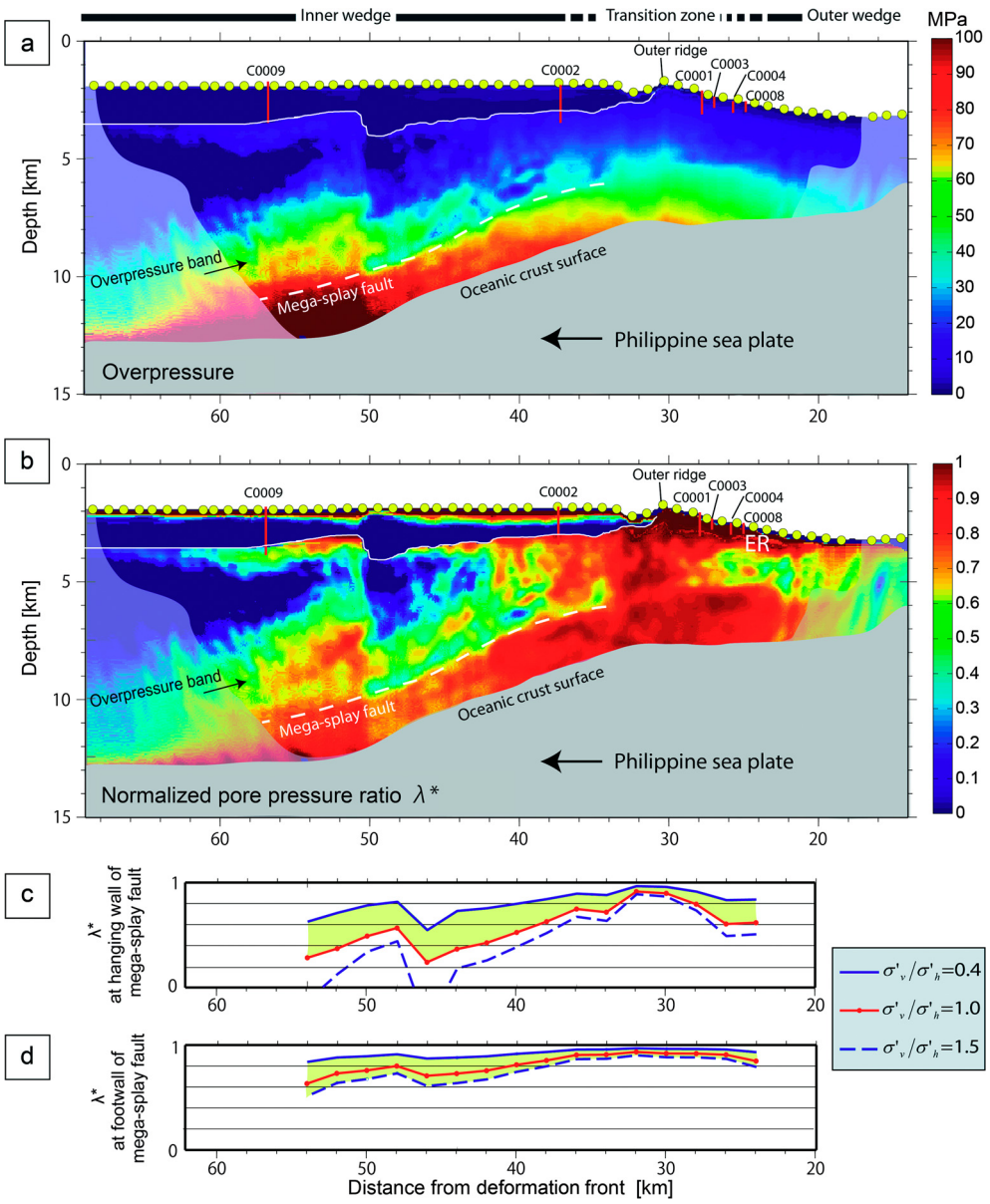

Fig. 4. (a) Overpressure calculated by subtracting hydrostatic pressure from the pore pressure estimated by fitting S-wave velocities. (b) Normalized pore pressure ratio distribution λ^*. (c) Normalized pore pressure ratio at the hanging wall of the mega-splay fault (from the accretionary prism surface to the mega-splay fault). (d) Normalized pore pressure ratio at the footwall of the mega-splay fault (from the mega-splay fault to the oceanic crust surface). (For interpretation of the references to color in this figure, the reader is referred to the web version of this article.)

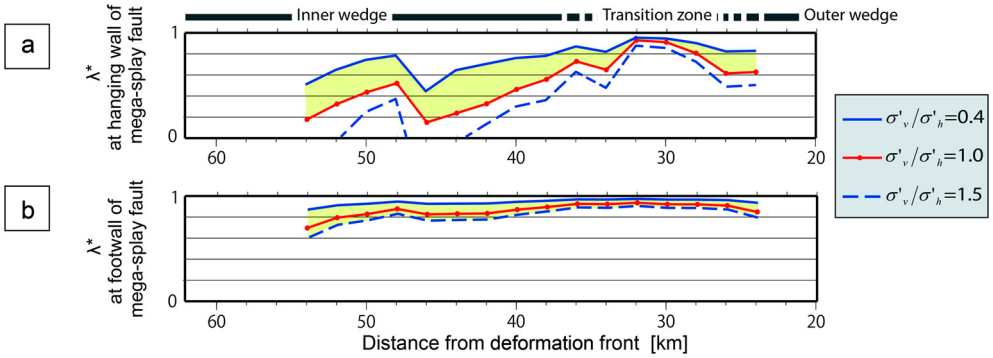

Fig. 5. (a) Normalized pore pressure ratio λ^* at the hanging wall of the mega-splay fault (from the accretionary prism surface to the mega-splay fault). (b) Normalized pore pressure ratio at the footwall of the mega-splay fault (from the mega-splay fault to the oceanic crust surface). Here we use different Vp/Vs ratio for hanging wall and footwall of the mega-splay fault by using information derived from AVO analysis of seismic reflections (see Fig. 2a). (For interpretation of the references to color in this figure, the reader is referred to the web version of this article.)

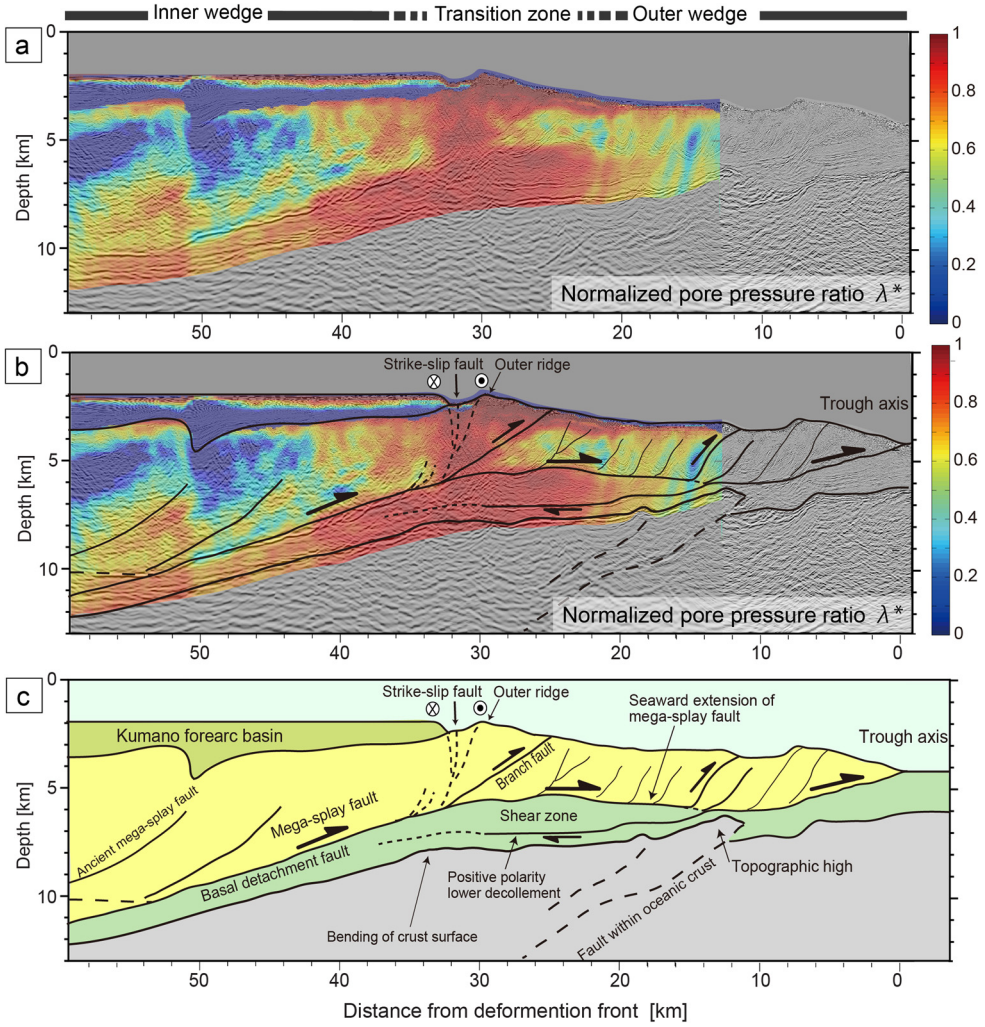

Fig. 6. (a) Normalized pore pressure ratio overlaid on the seismic reflection profile. The normalized pore pressure ratio is estimated from S-wave velocity (corresponding to Fig. 4b). (b) and (c) Interpretations of the mega-splay fault system from WT velocity profile and seismic reflection profile. Deeper part of the mega-splay fault continues to the seaward region and works as basal detachment fault.

To evaluate the estimated pore pressure distributions, we use the normalized pore pressure ratio

$$\lambda^* = \frac{(P_f - P_{hf})}{(P_c - P_{hf})}, \tag{5}$$

(see Figs. 3 to 5) where P_{hf} is the hydrostatic pressure (Screaton et al., 2002). The pore pressure estimated from the S-wave velocity (Fig. 4) is a little higher than that estimated from the P-wave velocity (Fig. 3). However the overall characteristics of the estimated pore pressure are similar around the mega-splay fault: the pore pressure on the footwall side of the mega-splay fault is consistently high within our analyzed area, and the pore pressure on the hanging wall is the highest at the transition zone (Fig. 6). In the footwall side, the pore pressure estimated from the separate S-wave velocities for the accretionary and underthrust sequences (Fig. 5b) is a little higher than that estimated from the average S-wave velocity within these sequences (Fig. 4d). We further observe high pore pressures at the footwall of each imbricate thrust in the outer wedge (Fig. 6).

3.3. Pore pressure estimated at inhomogeneous state of stress

In predicting pore pressure in the case of an inhomogeneous state of stress, we consider stress rather than pressure. The confining stress calculated by integrating the density in the depth direction is the vertical confining stress σ_v. To predict pore pressure from the vertical confining stress, Eq. (2) is rewritten as

$$\sigma'_v = \sigma_v - nP_f, \tag{6}$$

where σ'_v is the vertical effective stress. However, the effective stress estimated from seismic velocity roughly represents mean effective stress σ'_m.

By assuming that minimum σ'_3 and intermediate principal stresses σ'_2 are equal ($\sigma'_2 = \sigma'_3$), we can estimate the maximum and minimum principal stresses from the mean effective stress σ'_m using the ratio $R = \sigma'_3/\sigma'_1$ as follows:

$$\sigma'_1 = \frac{3}{1+2R}\sigma'_m, \tag{7}$$

$$\sigma'_3 = \frac{3R}{1+2R}\sigma'_m \tag{8}$$

(Moore and Tobin, 1997).

In the accretionary wedge where reverse faults are developed, the vertical effective stress σ'_v in Eq. (6) can be considered the minimum effective stress σ'_3 (Eq. (8) with $R_1 = \sigma'_v/\sigma'_h$) (Moore and Tobin, 1997; Moran et al., 1993), and we can estimate pore pressure as follows:

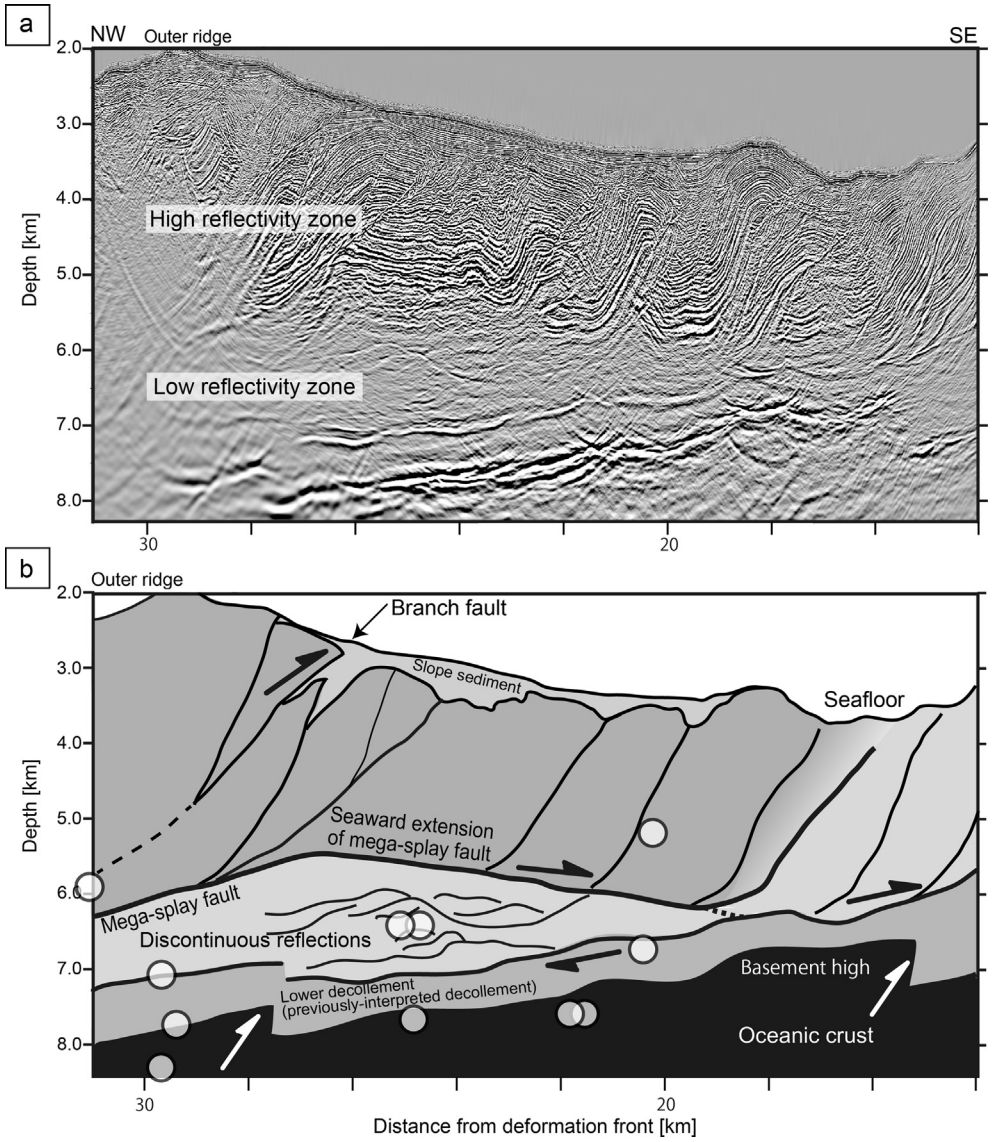

Fig. 7. (a) Seismic reflection profile showing discontinuous reflections within the abnormal pressure region seaward of outer ridge, and (b) its interpretation. This seismic profile showing clear discontinuous reflections is located at ~2 km east of the OBS survey line. White dots indicate the hypocenters of very low frequency earthquakes (Sugioka et al., 2012).

$$p_f = \frac{\sigma_v - (3R_1/(1+2R_1))\sigma'_m}{n},$$

$$R_1 = \frac{\sigma'_v}{\sigma'_h}. \tag{9}$$

$R_1 = \sigma'_v/\sigma'_h$ within the Nankai accretionary prisms was estimated at $\gtrsim$0.4 (e.g., Moran et al., 1993; Chang et al., 2010). Having obtained the mean effective stress σ'_m from seismic velocities, we can estimate pore pressure using Eq. (9). The normalized pore pressure ratios (Eq. (5)) are calculated for the hanging-wall of the mega-splay fault by assuming $R_1 = \sigma'_v/\sigma'_h = 0.4$ (solid blue lines in Figs. 3c, 4c, and 5a). The estimated pore pressure for $\sigma'_v/\sigma'_h = 0.4$ is higher than that of a homogeneous state of stress ($\sigma'_v/\sigma'_h = 1$). In the homogeneous stress condition ($\sigma'_v/\sigma'_h = 1$), the estimated pore pressures are lower than hydrostatic pressure at some parts of the accretionary prism (Kitajima and Saffer, 2012). As this sub-hydrostatic pressure condition is highly unrealistic, the σ'_v/σ'_h within the accretionary prism should be less than 1. Therefore, the probable range of normalized pore pressure ratio can be constrained to the yellow hatched area in Figs. 3c, 4c, and 5a.

In contrast, on the underthrust sequence on the footwall side of the mega-splay fault the vertical effective stress σ'_v is potentially larger than the horizontal stress σ'_h and can be considered to be the maximum stress σ'_1 (Eq. (7) with $R_2 = \sigma'_h/\sigma'_v$). In such a case, pore pressure can be estimated by using Eqs. (6) and (7) as follows:

$$p_f = \frac{\sigma_v - (3/(1+2R_2))\sigma'_m}{n},$$

$$R_2 = \frac{\sigma'_h}{\sigma'_v}. \tag{10}$$

Since the stress condition $R_2 = \sigma'_h/\sigma'_v$ in the underthrust sequence has not been well estimated, we calculate pore pressure for $R_2 = 0.67$ ($\sigma'_v/\sigma'_h = 1.5$). In this stress condition, the normalized pore pressure ratio on the footwall is slightly lower than in the homogeneous state of stress (dashed blue lines in Figs. 3d, 4d, and 5b). Note that the vertical effective stress σ'_v is potentially lower than horizontal stress σ'_h in the underthrust sequence also. Therefore, we estimate the uncertainty in normalized pore pressure ratio

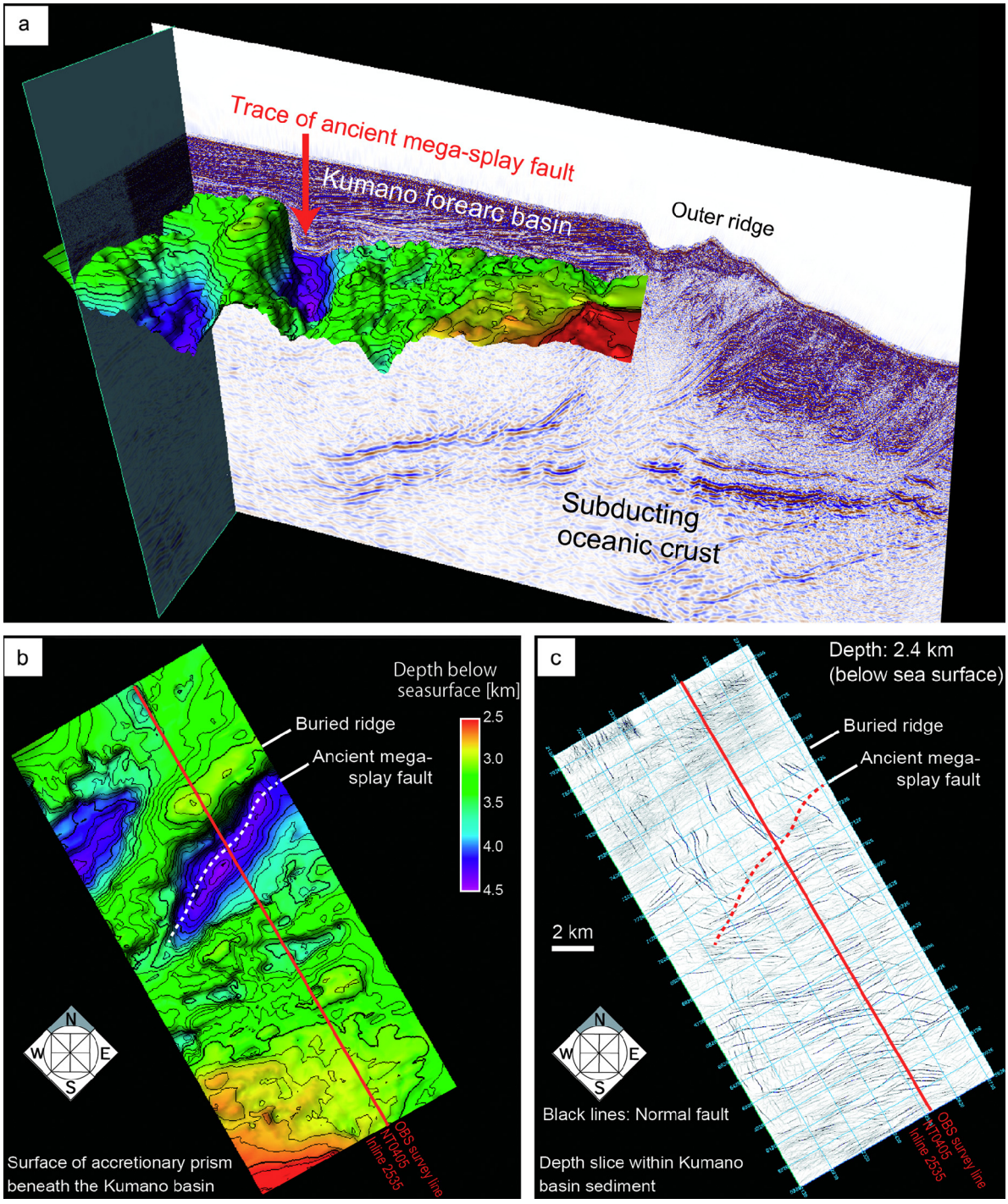

Fig. 8. (a) Subseafloor geometry of the top of the accretionary prism beneath the Kumano basin sediment, extracted from 3D seismic data (Moore et al., 2009). (b) Map view of the subseafloor geometry of top of the accretionary prism. The analyzed area is shown by a red rectangle in Fig. 1b. (c) Fault traces within Kumano basin sediment at the depth slice of 2400 m below the sea surface (~400 m below seafloor). Fault traces on this slice (black lines) are enhanced by seismic attributes (i.e., semblance). (For interpretation of the references to color in this figure legend, the reader is referred to the web version of this article.)

arising from the inhomogeneous state of stress as ±0.1 (yellow hatched area in Figs. 3d, 4d, and 5b).

3.4. Error in predicted pore pressure

Any pore pressure prediction method using seismic velocity has difficulty in distinguishing an overpressured zone from a possible fracture zone. Our approach considers that open fractures (cracks in our rock physics model) are supported by abnormal pressure, even if the fracture zone was constructed by past activity and is not presently supported by overpressure. However, open fractures along the fault plane are quickly sealed by mineral precipitation, once the fault becomes inactive. Therefore, any fractures revealed as high-pressure zones in our analysis should be recently generated due to fault activity.

In our pore pressure prediction, we assume that the velocity–pressure relationship is consistent between the Nobeoka thrust and the current mega-splay fault (Tsuji et al., 2006). The assumption may lead to some errors because the relationship between velocity and pressure is also influenced by the stress history of the rock

(e.g., Sarker and Batzle, 2008) and lithology. However, in the absence of direct measurements of the stress state and properties of the deeper part of the mega-splay fault, we consider the derived velocity–pressure relationship as a reasonable approximation of the current condition. Future drilling to the deep mega-splay fault will help in evaluating these errors and enable us to predict pore pressures more accurately.

As described in Section 3.1, the pore pressures estimated from the P-wave velocities (Fig. 3) may be less accurate for the deep rocks than those from the S-wave velocities (Fig. 4), due to the sensitivity to the effective-pressure coefficient; typically resulting in underestimation. Indeed the pore pressure predicted from the S-wave velocities (Fig. 4) is higher than that from the P-wave velocities (Fig. 3). For the shallow unconsolidated sediments, however, the S-wave velocity is almost zero, and the pore pressure predicted from the S-wave velocity is not accurate at shallow depths (labeled "ER" in Fig. 4b). Because the effective-pressure coefficient is almost 1 in the shallow region, pore pressure distribution estimated from P-wave velocity may be more reliable for shallow region (Fig. 3). However the crack model we used is not appropriate for unconsolidated materials (suited for the deep consolidated mega-splay fault region), therefore the pore pressures predicted from the P-wave velocity at the shallow depths still include some errors (labeled "ER" in Fig. 3b).

4. Discussion

4.1. Relationship between mega-splay fault and décollement

The pore pressure distribution we estimated in this study (Figs. 3–5) suggests that the zone of high pore pressure on the footwall side of the deeper part of the mega-splay fault continues seaward of the transition zone. This new interpretation (Fig. 6) for the mega-splay fault indicates that the top of the low-velocity zone identified by Park et al. (2010) corresponds to the seaward extension of the overpressure zone of the footwall of the mega-splay fault. Although there are some interpretations for the position of décollement in the outer wedge off Kumano based on the structural analysis (Park et al., 2002; Kington and Tobin, 2011; Moore et al., 2009), our predicted pore pressure strongly suggests that the main displacement plane (décollement) with large pore pressure contrast is located above the previously-interpreted décollement (e.g., Park et al., 2002) and continued from the mega-splay fault (Fig. 6).

The previously-interpreted décollement beneath the seaward extension of the mega-splay fault (approximately 1 km above the oceanic crust; Fig. 7) may function as the lower boundary of the overpressure zone, because its positive-polarity reflection indicates lower velocity on the hanging-wall side (Park et al., 2010). The reflection profile also displays discontinuous reflections within the high-pressure zone (Fig. 7). Therefore, the overpressure zone can be interpreted as a shear zone that may be a currently forming mélange or antiformal stacking (Park et al., 2010; Tsuji et al., 2007), and several dislocation planes are possibly developed in this zone. The seaward extension of the mega-splay fault is recognized on the reflection profile as a boundary between the high- and low-reflectivity zones (Fig. 7): the boundary is not imaged clearly in the profile potentially due to its heterogeneity (Kamei et al., 2012, 2013).

The reflection profile indicates that the seaward extension of the mega-splay fault branches upward to the seafloor, or merges downward into the previously-interpreted décollement about 14 km landward of the trench axis. The location corresponds to a topographic high in the oceanic crustal basement interpreted from the reflection profile (Figs. 6 and 7; Tsuji et al., 2009, 2013b). Velocity analysis of 3D multi-channel seismic reflection data also shows that the low-velocity zone is truncated at the basement high (Park et al., 2010). This result indicates that the shape of the crustal surface may have influenced the evolution of the fault.

4.2. Coseismic rupture propagation close to the trough region

The normalized pore pressure ratio λ^* of the footwall of the mega-splay fault is almost constant over the study region (20–60 km landward from the trough axis). The pore pressure estimated in our analysis (Figs. 3–5) is similar to that estimated using the velocity–porosity–effective stress relationships of sedimentary rocks on the incoming plate (Site C0011) by Kitajima and Saffer (2012). The pore pressure of the footwall of the mega-splay fault predicted from the S-wave velocity ($\lambda^* = 0.7$–0.95) is higher than that from the P-wave velocity, and we consider the estimation based on the S-wave velocity is more reliable as the effects of unknown effective pressure coefficient are limited. The pore pressure from the S-wave velocity is highest in the transition zone ($\sim$30 km from the trough axis) and slightly decreases landward (Figs. 4d and 5b). The region of the highest pore pressure ratio almost coincides with the hypocenters of the very low frequency earthquakes (Figs. 7; Ito and Obara, 2006; Sugioka et al., 2012; Kitajima and Saffer, 2012). The high pore pressures likely result from a combination of compaction disequilibrium and fluids released by clay dehydration (Moore and Vrolijk, 1992; Saffer and Tobin, 2011; Tsuji et al., 2008). The strong contrast in pore pressure at the mega-splay fault (Fig. 6) suggests poorly-drained conditions due to the presence of a low permeability layer along the fault plane (e.g., Brown et al., 1994).

The continuous high pore pressure beneath the mega-splay fault indicates the possibility of coseismic rupture propagation on the deep mega-splay fault as far as the trough region, as in the 1605 Keicho earthquake. Indeed, vitrinite reflectance geothermometry (Sakaguchi et al., 2011) showed evidence of the coseismic rupture out to the trough axis. We cannot find any significant pore pressure variation along the footwall that would act as a barrier for rupture propagation and set the updip limit of the seismogenic zone, although the study area includes the transition zone between coseismic and aseismic regions for the 1944 Tonankai earthquake (Kikuchi et al., 2003; Fig. 1).

If a coseismic rupture propagates close to the trough axis, the steep seafloor slope on the seaward side of the outer ridge moves seaward, and may contribute to large tsunamis, as in the 2011 Tohoku earthquake (Tanioka and Satake, 1996; Tsuji et al., 2013a). Park et al. (2010) also suggested that the uplift of the outer wedge contributed to tsunami generation during the 1944 Tonankai earthquake, based on the observation that the coseismic rupture area estimated from tsunami waveform inversion (Tanioka and Satake, 2001) extends further seaward than the rupture area estimated from coseismic waveform inversion (Kikuchi and Yamanaka, 2001).

4.3. Role of transition zone between inner and outer wedges

The pore pressure on the hanging-wall is the highest in the transition zone (Figs. 3c, 4c, 5a, 6), meaning that the difference in pore pressure across the fault is smallest there. This could influence the frictional characteristics along the fault plane and the rupture propagation pathway. The low pore pressure contrasts across the fault (or the high pore pressure at the hanging-wall side of the fault) may explain the branching of the mega-splay fault to the hanging-wall side in the transition zone. Therefore, the transition zone plays a key role in the rupture propagation and may control the up-dip limit of the seismogenic zone.

In addition, the shallow overpressured zone on the hanging wall beneath the outer ridge is possible to reflect the presence of open fractures. The fractures aligned along the outer ridge can be

also predicted from seismic anisotropy analysis (Tsuji et al., 2011). The fractures beneath the outer ridge may function as a strike-slip fault partitioning the strain arising from the oblique convergence of the subducting Philippine Sea plate (Ashi and et al., 2007; Martin et al., 2010; Fig. 6). The strain partitioning along strike-slip faults may also affect the stress orientation across the transition zone, as identified by borehole breakouts (e.g., Tobin et al., 2009; Lin et al., 2010), because strike-slip motion releases the subduction-normal stress due to the oblique plate subduction. Therefore, the strike-slip faults control the stress state within the accretionary prism and at the plate interface in the transition zone, and thus constitutes a key structure influencing the coseismic rupture propagation from the deep mega-splay fault to the trough.

4.4. Mega-splay fault working as basal detachment fault

At the landward side of the outer ridge (∼55 km from the trough axis; arrows in Figs. 3, 4), a belt of abnormal pore pressure is observed within the accretionary prism (i.e., the hanging-wall side) that soles into the present mega-splay fault (Fig. 6). This feature is also observed in the WT velocity model, and interpreted as a fault (Kamei et al., 2012). The subseafloor geometry of the top of the accretionary prism extracted from the 3D seismic reflection image (Figs. 8a and 8b) shows a ridge structure nearly parallel to, and with geometry similar to, the present outer ridge. The belt of abnormal pressure coincides with the location of the buried ridge, and thus may be interpreted as an ancient splay fault. This suggests in turn that the present active mega-splay fault observed as a strong amplitude reflection (Park et al., 2002) can be considered to be a basal detachment fault (i.e., a plate boundary décollement; Fig. 6), and that several faults are branched from the detachment fault and reach the sea floor.

It appears that the ancient mega-splay fault has recently been inactive, considering a lack of a dislocation plane due to fault activities in the shallow sediment of the Kumano forearc basin (Fig. 8c), and the difference in the strikes of the recent faults within the forearc basin and the ancient mega-splay fault (dashed line in Figs. 8b and 8c). Small deformation (suggested by a lack of a dislocation plane) in the post-Quarternary Kumano forearc sediment (Saffer and et al., 2009) further suggests that the ancient fault is not much active after ∼2 Ma. Since the time coincides with the initiation of the present mega-splay fault at the transition zone (Strasser et al., 2009; Kimura et al., 2011), the decrease in the ancient fault activity could be associated with the rupture propagation to the seaward present mega-splay fault. Furthermore, the activity of the present mega-splay fault slows down after 1.24 Ma, and the slip partition of the shallower part of mega-splay fault branched around the outer ridge is only ∼1.5–2.5% of the total plate convergence for dip direction (Kimura et al., 2011). These suggest that the large-part of displacement propagates to the seaward side. Gulick et al. (2010) further showed that strata in the Kumano forearc basin near the outer ridge were tilted during 1.3–1.0 Ma, due to the coseismic rupture along the mega-splay fault, and suggested that the majority of the slip has shifted to other faults, such as the décollement. This transient feature is consistent with our interpretation of the mega-splay fault working as a detachment fault (i.e., a plate boundary décollement).

5. Conclusions

We predict pore pressure distributions on the mega-splay fault in the Nankai Trough off Kumano, primarily based on the waveform tomography velocity by using rock physics to convert these velocities to pressure models. The high-resolution pore pressure obtained in this study (Fig. 6) provides new insights into the evolution of the mega-splay fault system.

Our primary conclusions are:

(1) The high pore pressures extend seaward along the footwall of the mega-splay fault to the trough region. The pore pressure of the footwall is close to lithostatic pressure, and the normalized pore pressure ratio is nearly constant within our study area.
(2) The continuous zone of the high pore pressure beneath the mega-splay fault across the transition zone supports the possibility of the coseismic rupture propagation closer to the trough than the currently interpreted mega-splay fault. The rupture propagation close to the trough axis potentially generates a huge tsunami.
(3) The high pressure belt within the accretionary wedge on the landward side of the present mega-splay fault may be interpreted as the ancient mega-splay fault.
(4) The presently active mega-splay fault with a strong reflection amplitude serves as a basal detachment fault (i.e., a plate boundary décollement), and the several faults are branched from the basal detachment fault.
(5) The relatively low contrast in pore pressure across the fault in the transition zone between the inner and outer wedge could influence the rupture propagation pathway. The pore pressure could control whether a coseismic rupture propagates to the trough region or branches up to the seafloor at the transition zone.
(6) The shallow overpressured zone beneath the transition zone could partially reflect the presence of open fractures associated with a strike-slip fault. The strain partitioning due to strike-slip motions influences to the stress state along the detachment fault, constituting a key structure influencing the coseismic rupture.

Acknowledgements

We used logging data provided by IODP, and OBS data provided by Japan Agency for Marine–Earth Science and Technology. We thank J. Ashi (Univ. Tokyo) for discussions. A. Shulgin and two anonymous reviewers gave us constructive comments. This study was supported by a Grant-in-Aid for Scientific Research on Innovative Areas from the JSPS (21107003). T. Tsuji gratefully acknowledges the support of the International Institute for Carbon Neutral Energy Research (WPI-I2CNER), sponsored by the World Premier International Research Center Initiative (WPI), MEXT, Japan.

References

Ando, M., 1975. Source mechanisms and tectonic significance of historical earthquake derived from tsunami data. Phys. Earth Planet. Inter. 28, 320–336.
Ashi, J., et al., 2007. NanTroSEIZE Stage 1: NanTroSEIZE megasplay riser pilot [online]. In: IODP Sci. Prosp., vol. 315, 78 pp. http://dx.doi.org/10.2204/iodp.sp.315.2007. Available at: http://publications.iodp.org/scientific_prospectus/315/315SP.PDF.
Bangs, N.L., Shipley, T.H., Moore, J.C., Moore, G.F., 1999. Fluid accumulation and channeling along the northern Barbados Ridge décollement thrust. J. Geophys. Res. 104, 20,399–20,414.
Bangs, N., Moore, G., Gulick, S., Pangborn, E., Tobin, H., Kuramoto, S., Taira, A., 2009. Broad, weak regions of the Nankai megathrust and implications for shallow coseismic slip. Earth Planet. Sci. Lett. 284, 44–49.
Berryman, J.G., 1992. Single-scattering approximations for coefficients in Biot's equations of poroelasticity. J. Acoust. Soc. Am. 91, 551–571.
Biot, M.A., 1955. Theory of elasticity and consolidation for a porous anisotropic solid. J. Appl. Phys. 26, 115–135.
Biot, M.A., Willis, D.G., 1957. The elastic coefficients of the theory of consolidation. J. Appl. Mech. 24, 594–601.
Brenders, A.J., Pratt, R.G., 2007. Full waveform tomography for lithospheric imaging: results from a blind test in a realistic crustal model. Geophys. J. Int. 168, 133–151.
Brown, K.M., Bekins, B., Clennell, B., Dewhurst, D., Westbrook, G., 1994. Heterogeneous hydrofracture development and accretionary fault dynamics. Geology 22, 259–262.
Carcione, J.M., Helle, H.B., Pham, N.H., Toverud, T., 2003. Pore pressure estimation in reservoir rocks from seismic reflection data. Geophysics 68, 1569–1579.

Chang, C., McNeill, L.C., Moore, J.C., Lin, W., Conin, M., Yamada, Y., 2010. In situ stress state in the Nankai accretionary wedge estimated from borehole wall failures. Geochem. Geophys. Geosyst. 11, Q0AD04. http://dx.doi.org/10.1029/2010GC003261.

Cheng, C.H., Toksoz, M.N., 1979. Inversion of seismic velocities for the pore aspect ratio spectrum of a rock. J. Geophys. Res. 84, 7533–7543.

Cochrane, G.R., Moore, J.C., MacKay, M.E., Moore, G.F., 1994. Velocity and inferred porosity model of the Oregon accretionary prism from multichannel seismic reflection data: implications on sediment dewatering and overpressure. J. Geophys. Res. 99, 7033–7043.

Christensen, N.I., Wang, H.F., 1985. The influence of pore pressure and confining pressure on dynamic elastic properties of Berea sandstone. Geophysics 50, 207–213.

Conin, M., Henry, P., Godard, V., Bourlange, S., 2012. Splay fault slip in a subduction margin, a new model of evolution. Earth Planet. Sci. Lett. 341–344, 170–175.

Dvorkin, J., Mavko, G., Nur, A., 1999. Overpressure detection from compressional- and shear-wave data. Geophys. Res. Lett. 26, 3417–3420. http://dx.doi.org/10.1029/1999GL008382.

Dutta, N.C., 2001. Geopressure prediction using seismic data: current status and the road ahead. Geophysics 67, 2012–2041.

Eaton, B.A., 1972. Graphical method predicts geopressures worldwide. World Oil 182 (6), 51–56.

Eberhart-Phillips, D., Han, D., 1989. Empirical relationships among seismic velocity, effective pressure, porosity and clay content in sand-stone. Geophysics 54, 82–89.

Fujiwara, T., Kodaira, S., No, T., Kaiho, Y., Takahashi, N., Kaneda, Y., 2011. The 2011 Tohoku-Oki earthquake: displacement reaching the trench axis. Science 334, 1240.

Gangi, A.F., Carlson, R.L., 1996. An asperity-deformation model for effective pressure. Tectonophysics 256, 241–251.

Gulick, S.P.S., Bangs, N., Moore, G.F., Ashi, J., Martin, K.M., Sawyer, D.S., Tobin, H.J., Kuramoto, S., Taira, A., 2010. Rapid forearc basin uplift and megasplay fault development from 3D seismic images of Nankai Margin off Kii Peninsula, Japan. Earth Planet. Sci. Lett. 300, 55–62.

Hamahashi, M., et al., 2013. Contrasts in physical properties between the hanging wall and footwall of an exhumed seismogenic megasplay fault in a subduction zone – an example from the Nobeoka thrust drilling project. Geochem. Geophys. Geosyst. 14. http://dx.doi.org/10.1002/2013GC004818.

Hashimoto, Y., Tobin, H.J., Knuth, M., 2010. Velocity–porosity relationships for slope apron and accreted sediments in the Nankai Trough Seismogenic Zone Experiment, Integrated Ocean Drilling Program Expedition 315 Site C0001. Geochem. Geophys. Geosyst. 11, Q0AD05. http://dx.doi.org/10.1029/2010GC003217.

Hayward, N., Westbrook, G.K., Peacock, S., 2003. Seismic velocity, anisotropy, and fluid pressure in the Barbados accretionary wedge from an offset vertical seismic profile with seabed sources. J. Geophys. Res. 108 (B11), 2515. http://dx.doi.org/10.1029/2001JB001638.

Hoffman, N.W., Tobin, H.J., 2004. An empirical relationship between velocity and porosity for underthrust sediments in the Nankai Trough accretionary prism. In: Mikada, H., Moore, G.F., Taira, A., Becker, K., Moore, J.C., Klaus, A. (Eds.), Proc. ODP, Sci. Results, vol. 190/196, pp. 1–23.

Hoffmann, R., Xu, X., Batzle, M., Prasad, M., Furre, A.-K., Pillitteri, A., 2005. Effective pressure or what is the effect of pressure? Lead. Edge 24, 1256–1260.

Ishibashi, K., 1983. Tectonic significance of the 1605 Keicho tsunami earthquake off Tokai-Nankai, Japan. Abstr. Seism. Soc. Jpn. 1, 96 (in Japanese).

Ito, Y., Tsuji, T., Osada, Y., Kido, M., Inazu, D., Hayashi, Y., Tsushima, H., Hino, R., Fujimoto, H., 2011. Frontal wedge deformation near the source region of the 2011 Tohoku-Oki earthquake. Geophys. Res. Lett. 38, L00G05. http://dx.doi.org/10.1029/2011GL048355.

Ito, Y., Obara, K., 2006. Dynamic deformation of the accretionary prism excites very low frequency earthquakes. Geophys. Res. Lett. 33, L02311. http://dx.doi.org/10.1029/2005GL025270.

Kamei, R., Pratt, R.G., Tsuji, T., 2012. Waveform tomography imaging of a megasplay fault system in the seismogenic Nankai subduction zone. Earth Planet. Sci. Lett. 317–318, 343–353.

Kamei, R., Pratt, R.G., 2012. Wide-band multifrequency waveform inversion in the Laplace–Fourier domain. In: SEG Technical Program Expanded Abstracts, pp. 1–6.

Kamei, R., Pratt, R.G., Tsuji, T., 2013. On acoustic waveform tomography of wide-angle OBS data – strategies for preconditioning and inversion. Geophys. J. Int. 194, 1250–1280. http://dx.doi.org/10.1093/gji/ggt165.

Kikuchi, M., Nakamura, M., Yoshikawa, K., 2003. Source rupture processes of the 1944 Tonankai earthquake and the 1945 Mikawa earthquake derived from low-gain seismograms. Earth Planets Space 55, 159–172.

Kikuchi, M., Yamanaka, Y., 2001. Rupture process of great earthquakes: identification of asperity. Seismo 7, 6–7.

Kimura, G., Moore, G.F., Strasser, M., Screaton, E., Curewitz, D., Streiff, C., Tobin, H., 2011. Spatial and temporal evolution of the megasplay fault in the Nankai Trough. Geochem. Geophys. Geosyst. 12, Q0A008. http://dx.doi.org/10.1029/2010GC003335.

Kimura, G., Hina, S., Hamada, Y., Kameda, J., Tsuji, T., Kinoshita, M., Yamaguchi, A., 2012. Runaway slip to the trench due to rupture of highly pressurized megathrust beneath the middle trench slope: the tsunamigenesis of the 2011 Tohoku earthquake off the east coast of northern Japan. Earth Planet. Sci. Lett. 339–340, 32–45.

Kington, J.D., Tobin, H.J., 2011. Balanced cross sections, shortening estimates, and the magnitude of out-of-sequence thrusting in the Nankai Trough accretionary prism, Japan. In: 2011 Fall Meeting. AGU, San Francisco, CA, 5–9 Dec. Abstract T21B-2364.

Kitajima, H., Saffer, D.M., 2012. Elevated pore pressure and anomalously low stress in regions of low frequency earthquakes along the Nankai Trough subduction megathrust. Geophys. Res. Lett. 39, L23301. http://dx.doi.org/10.1029/2012GL053793.

Kondo, H., et al., 2005. Deformation and fluid flow of a major out-of-sequence thrust located at seismogenic depth in an accretionary complex: Nobeoka Thrust in the Shimanto Belt, Kyusyu, Japan. Tectonics 24, TC6008. http://dx.doi.org/10.1029/2004TC001655.

Kopp, H., 2013. Invited review paper: the control of subduction zone structural complexity and geometry on margin segmentation and seismicity. Tectonophysics 589, 1–16.

Kopp, H., Hindle, D., Klaeschen, D., Oncken, O., Reichert, C., Scholl, D., 2009. Anatomy of the western Java plate interface from depth-migrated seismic images. Earth Planet. Sci. Lett. 288, 399–407.

Kuster, G.T., Toksoz, M.N., 1974. Velocity and attenuation of seismic waves in two-phase media, Part 1 – Theoretical formulations. Geophysics 39, 587–606.

Lin, W., et al., 2010. Present-day principal horizontal stress orientations in the Kumano forearc basin of the southwest Japan subduction zone determined from IODP NanTroSEIZE drilling Site C0009. Geophys. Res. Lett. 37 (13), L13303. http://dx.doi.org/10.1029/2010GL043158.

Martin, K.M., et al., 2010. Possible strain partitioning structure between the Kumano fore-arc basin and the slope of the Nankai Trough accretionary prism. Geochem. Geophys. Geosyst. 11, Q0AD02. http://dx.doi.org/10.1029/2009GC002668.

Mavko, G., Mukerji, T., Dvorkin, J., 1998. The Rock Physics Handbook, Tool for Seismic Analysis in Porous Media. Cambridge University Press, UK.

Miyazaki, S., Heki, K., 2001. Crustal velocity field of southwest Japan: Subduction and arc–arc collision. J. Geophys. Res. 106, 4305–4326.

Moore, G., et al., 2009. Structural and seismic stratigraphic framework of the NanTroSEIZE Stage 1 transect. In: Proc. IODP, vols. 314/315/316. College Station, TX.

Moore, J.C., Vrolijk, P., 1992. Fluids in acretionary prisms. Rev. Geophys. 30 (2), 113–135. http://dx.doi.org/10.1029/92RG00201.

Moore, J.C., Tobin, H., 1997. Estimated fluid pressures of the Barbados accretionary prism and adjacent sediments. In: Shipley, T.H., Ogawa, Y., Blum, P., Bahr, J.M. (Eds.), Proc. ODP, Sci. Results, vol. 156, pp. 229–238.

Moore, J.C., Saffer, D.M., 2001. Updip limit of the seismogenic zone beneath the accretionary prism of southwest Japan: an effect of diagenetic to low-grade metamorphic processes and increasing effective stress. Geology 29, 183–186.

Moran, K., Bruckmann, W., Feeser, V., Campanella, R.G., 1993. In situ stress conditions at Nankai Trough Site 808. In: Fill, I.A., Taira, A., Firth, J.V., et al. (Eds.), Proc. ODP, Sci. Results, vol. 131. College Station (Ocean Drilling Program), TX, pp. 283–291.

Morgan, J.K., Ramsey, E.B., Ask, M.V.S., 2007. Deformation and mechanical strength of sediments at the Nankai subduction zone. In: Dixon, T.H., Moore, J.C. (Eds.), The Seismogenic Zone of Subduction Thrust Faults. Columbia Press, New York, pp. 210–256.

Nakanishi, A., et al., 2008. Detailed structural image around splay-fault branching in the Nankai subduction seismogenic zone: results from a high-density ocean bottom seismic survey. J. Geophys. Res. 113, B03105. http://dx.doi.org/10.1029/2007JB004974.

Powers, M.C., 1959. Adjustment of clays to chemical charge and the concept of the equivalence level. In: Clays Clay Miner., vol. 2. Pergamon Press, New York, pp. 309–326.

Park, J.-O., Tsuru, T., Kodaira, S., Cummins, P.R., Kaneda, Y., 2002. Splay fault branching along the Nankai Subduction zone. Science 297, 1157–1160.

Park, J.-O., et al., 2010. A low-velocity zone with weak reflectivity along the Nankai subduction zone. Geology 38, 283–286.

Prasad, M., Manghnani, M.H., 1997. Effects of pore and differential pressure on compressional wave velocity and quality factor in Berea and Michigan sandstones. Geophysics 62, 1163–1176. http://dx.doi.org/10.1190/1.1444217.

Ranero, C.R., von Huene, R., 2000. Subduction erosion along the Middle America convergent margin. Nature 404, 748–752.

Raimbourg, H., Hamano, Y., Saito, S., Kinoshita, M., Kopf, A., 2011. Acoustic and mechanical properties of Nankai accretionary prism core samples. Geochem. Geophys. Geosyst. 12, Q0AD10. http://dx.doi.org/10.1029/2010GC003169.

Rubey, W.W., Hubbert, M.K., 1959. Overthrust belt in geosynclinal area of western Wyoming in light of fluid pressure hypothesis, 2: Role of fluid pressure in mechanics of overthrust faulting. Geol. Soc. Am. Bull. 70, 167–206.

Ryan, H., von Huene, R., Scholl, D., Kirby, S., 2012. Tsunami hazards to U.S. coasts from giant earthquakes in Alaska. Eos Trans. AGU 93 (19), 185. http://dx.doi.org/10.1029/2012EO190001.

Saffer, D.M., 2003. Pore pressure development and progressive dewatering in underthrust sediments at the Costa Rican subduction margin: comparison with northern Barbados and Nankai. J. Geophys. Res. 108 (B5), 2261. http://dx.doi.org/10.1029/2002JB001787.

Saffer, D., et al., 2009. NanTroSEIZE Stage 2: NanTroSEIZE riser/riserless observatory. In: IODP Prel. Rept., vol. 319. http://dx.doi.org/10.2204/iodp.pr.319.2009.

Saffer, D.M., Tobin, H.J., 2011. Hydrogeology and mechanics of subduction zone forearcs: fluid flow and pore pressure. Annu. Rev. Earth Planet. Sci. 39, 157–186.

Sakaguchi, S., et al., 2011. Seismic slip propagation to the updip end of plate boundary subduction interface faults: vitrinite reflectance geothermometry on Integrated Ocean Drilling Program NanTro SEIZE cores. Geology 39, 395–398.

Sarker, R., Batzle, M., 2008. Effective stress coefficient in shales and its applicability to Eaton's equation. Lead. Edge 27 (6), 798–804.

Satake, K., 1994. Mechanism of the 1992 Nicaragua tsunami earthquake. Geophys. Res. Lett. 21, 2519–2522.

Scholz, C.H., 1998. Earthquakes and friction lows. Nature 391, 37–42.

Screaton, E., Saffer, D., Henry, P., Hunze, S., Leg 190 Shipboard Scientific Party, 2002. Porosity loss within the underthrust sediments of the Nankai accretionary complex: Implications for overpressure. Geology 30, 19–22.

Seno, T., Stein, S., Gripp, A.E., 1993. A model for the motion of the Philippine Sea plate consistent with NUVEL-1 and geological data. J. Geophys. Res. 98, 17,941–17,948.

Seno, T., 2002. Tsunami earthquakes as transient phenomena. Geophys. Res. Lett. 29. http://dx.doi.org/10.1029/2002GL014868.

Shipley, T.H., Moore, G.F., Bangs, N.L., Moore, J.C., Stoffa, P.L., 1994. Seismically inferred dilatancy distribution, northern Barbados Ridge decollement: implications for fluid migration and fault strength. Geology 22, 411–414.

Strasser, M., Moore, G.F., Kimura, G., Kitamura, Y., Kopf, A., Lallemant, S., Park, J.-O., Screaton, E.J., Su, X., Underwood, M.B., Zhao, X., 2009. Origin and evolution of a splay fault in the Nankai accretionary wedge. Nat. Geosci. 2, 648–652. http://dx.doi.org/10.1038/ngeo609.

Sugioka, H., Okamoto, T., Nakamura, T., Ishihara, Y., Ito, A., Obana, K., Kinoshita, M., Nakahigashi, K., Shinohara, M., Fukao, Y., 2012. Tsunamigenic potential of the shallow subduction plate boundary inferred from slow seismic slip. Nat. Geosci. 5, 414–418. http://dx.doi.org/10.1038/ngeo1466.

Takahashi, N., et al., 2002. Seismic structure of western end of the Nankai trough seismogenic zone. J. Geophys. Res. 107 (B10), 2212–2230. http://dx.doi.org/10.1029/2000JB000121.

Tanioka, Y., Satake, K., 1996. Tsunami generation by horizontal displacement of ocean bottom. Geophys. Res. Lett. 23, 861–864.

Tanioka, Y., Satake, K., 2001. Detailed coseismic slip distribution of the 1944 Tonankai earthquake estimated from tsunami waveforms. Geophys. Res. Lett. 28, 1075–1078. http://dx.doi.org/10.1029/2000GL012284.

Terzaghi, K., 1936. The shear resistance of saturated soils. In: Proceedings for the 1st International Conference on Soil Mechanics and Foundation Engineering, vol. 1. Cambridge, MA, pp. 54–56.

Tobin, H., et al., 2009. Expedition 314 summary. In: NanTroSEIZE Stage 1: Investigations of Seismogenesis, Nankai Trough, Japan. In: Proc. Integr. Ocean Drill. Program, vols. 314/315/316. http://dx.doi.org/10.2204/iodp.proc.314315316.111.2009.

Tobin, H., Saffer, D., 2009. Elevated fluid pressure and extreme mechanical weakness of a plate boundary thrust, Nankai Trough subduction zone. Geology 37, 679–682.

Toksoz, M.N., Cheng, C.H., Timur, A., 1976. Velocity of seismic waves in porous rocks. Geophysics 41, 621–645.

Tsuji, T., Kawamura, K., Kanamatsu, T., Kasaya, T., Fujikura, K., Ito, Y., Tsuru, T., Kinoshita, M., 2013a. Extension of continental crust by anelastic deformation during the 2011 Tohoku-Oki earthquake: the role of extensional faulting in the generation of a great tsunami. Earth Planet. Sci. Lett. 364, 44–58. http://dx.doi.org/10.1016/j.epsl.2012.12.038.

Tsuji, T., Kodaira, S., Ashi, J., Park, J.-O., 2013b. Widely distributed thrust and strike-slip faults within subducting oceanic crust in the Nankai Trough off the Kii Peninsula, Japan. Tectonophysics 600, 52–62. http://dx.doi.org/10.1016/j.tecto.2013.03.014.

Tsuji, T., et al., 2011. Vp/Vs ratio and shear-wave splitting in the Nankai Trough seismogenic zone: insights into effective stress, pore pressure and sediment consolidation. Geophysics 76 (3), WA71–WA82.

Tsuji, T., Park, J.-O., Moore, G., Kodaira, S., Fukao, Y., Kuramoto, S., Bangs, N., 2009. Intraoceanic thrusts in the Nankai Trough off the Kii Peninsula: implications for intraplate earthquakes. Geophys. Res. Lett. 36, L06303. http://dx.doi.org/10.1029/2008GL036974.

Tsuji, T., Tokuyama, H., Costa Pisani, P., Moore, G., 2008. Effective stress and pore pressure in the Nankai accretionary prism off the Muroto Peninsula, southwestern Japan. J. Geophys. Res. 113, B11401. http://dx.doi.org/10.1029/2007JB005002.

Tsuji, T., Iturrino, G., 2008. Velocity–porosity relationships of oceanic basalt from eastern flank of the Juan de Fuca ridge: the effect of crack closure on seismic velocity. Explor. Geophys. 39, 41–51.

Tsuji, T., Park, J.-O., Moore, G., Kodaira, S., Kuramoto, S., Bangs, N., Yamada, Y., Matsuoka, T., 2007. Tectonic underplating in the Nankai Trough off the Kii peninsula: insight from Kumano 3D seismic reflection data. Eos Trans. AGU 88 (52). Fall Meet. Suppl., Abstract T51C-0697.

Tsuji, T., Kimura, G., Okamoto, S., Kono, F., Mochinaga, H., Saeki, T., Tokuyama, H., 2006. Modern and ancient seismogenic out-of-sequence thrusts in the Nankai accretionary prism: comparison of laboratory-derived physical properties and seismic reflection data. Geophys. Res. Lett. 33, L18309. http://dx.doi.org/10.1029/2006GL027025.

Tsuru, T., Miura, S., Park, J.-O., Ito, A., Fujie, G., Kaneda, Y., No, T., Katayama, T., Kasahara, J., 2005. Variation of physical properties beneath a fault observed by a two-ship seismic survey off southwest Japan. J. Geophys. Res. 110, B05405. http://dx.doi.org/10.1029/2004JB003036.

Van Avendonk, H.J.A., Gulick, S.P.S., Christeson, G.L., Worthington, L.L., Pavlis, T.L., Ridgway, K.D., 2013. Subduction and accretion of sedimentary rocks in the Yakutat collision zone, St. Elias orogen, Gulf of Alaska. Earth Planet. Sci. Lett. 381, 116–126.

von Huene, R., Lee, H., 1982. The possible significance of pore fluid pressures in subduction zones. In: Watkins, J.S., Drake, C.L. (Eds.), Studies in Continental Margin Geology. In: AAPG Mem., vol. 34, pp. 781–791.

Wang, K., Hu, Y., 2006. Accretionary prism in subduction earthquake cycles: the theory of dynamic Coulomb wedge. J. Geophys. Res. 111, B06410. http://dx.doi.org/10.1029/2005JB004094.

Wang, Z., 2001. Fundamentals of seismic rock physics. Geophysics 66, 398–412.

Westbrook, G.K., 1991. Geophysical evidence for the role of fluids in accretionary wedge tectonics. Philos. Trans. R. Soc. Lond. Ser. A 335, 227–242.

Yilmaz, O., Doherty, S., 2001. Seismic Data Processing, 2nd ed. Invest. in Geophys. SEG, Tulsa, Okla.